Swiss Journal of Geosciences (2018) 111:573–588
https://doi.org/10.1007/s00015-018-0309-4

Flooding a landscape: impact of Holocene transgression on coastal sedimentology and underwater archaeology in Kiladha Bay (Greece)

Morgane Surdez[1] · Julien Beck[2] · Dimitris Sakellariou[3] · Hendrik Vogel[1] · Patrizia Birchler Emery[2] · Despina Koutsoumba[4] · Flavio S. Anselmetti[1]

Received: 21 September 2017 / Accepted: 23 March 2018 / Published online: 3 May 2018

Abstract
Franchthi Cave, bordering Kiladha Bay, in Greece, is a key archaeological site, due to its long occupation time, from ~ 40,000 to ~ 5000 year BP. To date, no clear evidence of Neolithic human dwellings in the cave was found, supporting the assumption that Neolithic people may have built a village where there is now Kiladha Bay. During the Neolithic period/Early Holocene, wide areas of the bay were indeed emerged above sea level. Bathymetric and seismic data identified a terrace incised by a valley in ~ 1 to 2 m sediment depth. Eight sediment cores, up to 6.3-m-long, were retrieved and analysed using petrophysical, sedimentological, geochemical, and chronostratigraphic methods. The longest core extends into the exposure surface, consisting of a layer of carbonate rubble in a finer matrix, representing weathering processes. Dated organic remains place this unit at ~ 8500 cal year BP. It is overlain by stiff silty mud representing an estuarine environment. This mud is capped by reduced sediments with roots marking an exposure surface. A shell-layer, dated to ~ 6300 cal year BP, overlies this terrestrial sequence, reflecting the marine transgression. This layer occurs at 10.8 mbsl, 7.7 m deeper than the global sea level at that time, suggesting tectonic subsidence in the area. It is overlain by finer-grained marine carbonate-rich sediments. The top of the core shows traces of eutrophication, pebbles and marine shells, all likely a result of modern anthropogenic processes. These results are interpreted in the context of human occupation: the exposed surface contains pottery sherds, one dating to the Early to Middle Neolithic period, indicating that Neolithic people were present in this dynamic landscape interacting with a migrating coastline. Even if the artefacts are isolated, future investigations of the submerged landscape off Franchthi Cave might lead to the discovery of a Neolithic village, which eventually became buried under marine sediments.

Keywords Shallow marine sediments · Submerged prehistoric landscapes · Franchthi Cave · Argolic Gulf · Tectonic subsidence

1 Introduction

1.1 Archaeological context, sea-level changes since the Last Glacial Maximum and submerged prehistoric landscapes

First evidence for agriculture was found in the Near East around 12,000 year ago (Simmons 2007). This new lifestyle, termed Neolithic, was accompanied by the emergence of structured and long-term settlements. From the Near East, the Neolithic culture propagated towards Europe along different routes. One of the earliest dates for the Neolithic in Europe (~ 9000 year BP) was discovered in Franchthi Cave (Perlès et al. 2013), a major archaeological site bordering Kiladha Bay in the Argolid, Greece (Fig. 1).

Editorial handling: W. Winkler.

✉ Morgane Surdez
morgane.surdez@unifr.ch

[1] Institute of Geological Sciences and Oeschger Centre for Climate Change Research, University of Bern, Bern, Switzerland

[2] Département des Sciences de l'Antiquité, University of Geneva, Geneva, Switzerland

[3] Institute of Oceanography, Hellenic Centre for Marine Research, Anavyssos, Greece

[4] Ephorate of Underwater Antiquities, Hellenic Ministry of Culture and Sports, Athens, Greece

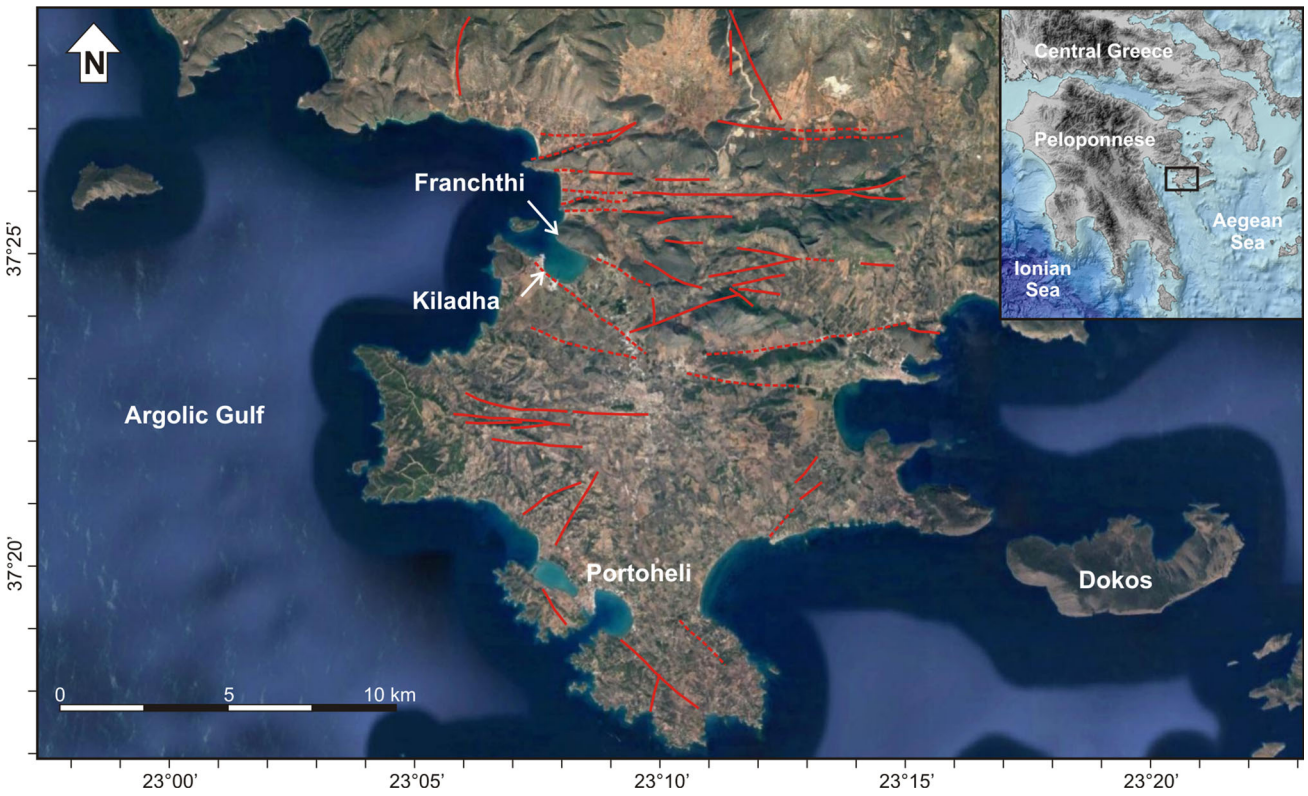

Fig. 1 Google earth image of the Southern Argolid, Greece, with main faults after Bannert (1977) and Gaitanakis and Fotiades (2007)

This cave was excavated by archaeologists led by T. W. Jacobsen (Indiana University, USA) in the 1960s and 1970s. Besides a large rockfall from the roof that likely occurred around the end of the Neolithic occupation of the cave (Farrand 2000), the cave shows traces of human presence from ~ 40,000 to ~ 5000 year BP, making it one of the longest occupied archaeological sites in Europe (Farrand 2000). However, there is no clear evidence that the cave was used as a dwelling place during the Neolithic, although there were signs of human activity from this period. Excavations on the shore between the cave and the bay, on the so-called "Paralia" sector, revealed the presence of Neolithic walls and other archaeological remains, yet still no clear evidence of habitation was found (Wilkinson and Duhon 1990). Therefore, archaeologists made the assumption that Neolithic people may have built a village further away from the cave, where there is now the bay, a place which is today submerged below ~ 2 to 14 m of water, but which was at that time exposed due to lower than present sea level (Wilkinson and Duhon 1990; Lambeck 1996).

During the Last Glacial Maximum (LGM), global sea level was ~ 120 to 130 m below today's level (van Andel and Lianos 1983; Lambeck et al. 2014), with large shelf areas being exposed. With the melting of the large continental ice-sheets, global sea level rose up to present level, causing a landward migration of the shorelines. Because sea level was below present for most of human history, many archaeological sites may today be submerged, as investigated in various studies (e.g. van Andel 1989; Bailey and Flemming 2008; Mourtzas and Kolaiti 2013; Pavlopoulos et al. 2013; Sakellariou et al. 2015; Sakellariou and Galanidou 2015; Weiberg et al. 2016; Avramidis et al. 2017). For this reason, geophysical surveys of Kiladha Bay were performed in 1979 and 1981 (e.g. van Andel et al. 1980; van Andel and Lianos 1983; van Andel 1987) to recover high-resolution seismic reflection and side-scan sonar data of the submerged landscape. This was complemented by the retrieval of sediment cores in 1981 and 1985, in which pottery sherds as well as other cultural indicators (e.g. stone artefacts, seeds of domesticated plant, etc.) were discovered (Gifford 1983; Wilkinson and Duhon 1990). These investigations proposed a reconstruction of the evolution of the coastal environment after the LGM.

The lack of detailed positioning, state-of-the-art bathymetric and seismic data as well as detailed sediment core analysis of the earlier surveys left many questions unaddressed. In order to refine the results obtained in the 1970s–1980s, research in Kiladha Bay resumed in 2012 (the Bay of Kiladha project) with updated technologies. The 2014 Terra Submersa expedition investigated Kiladha Bay with modern seismic and bathymetric tools (Sakellariou et al. 2015; Beck et al. 2017). Simultaneously, a submarine archaeological survey led to the discovery of a submerged

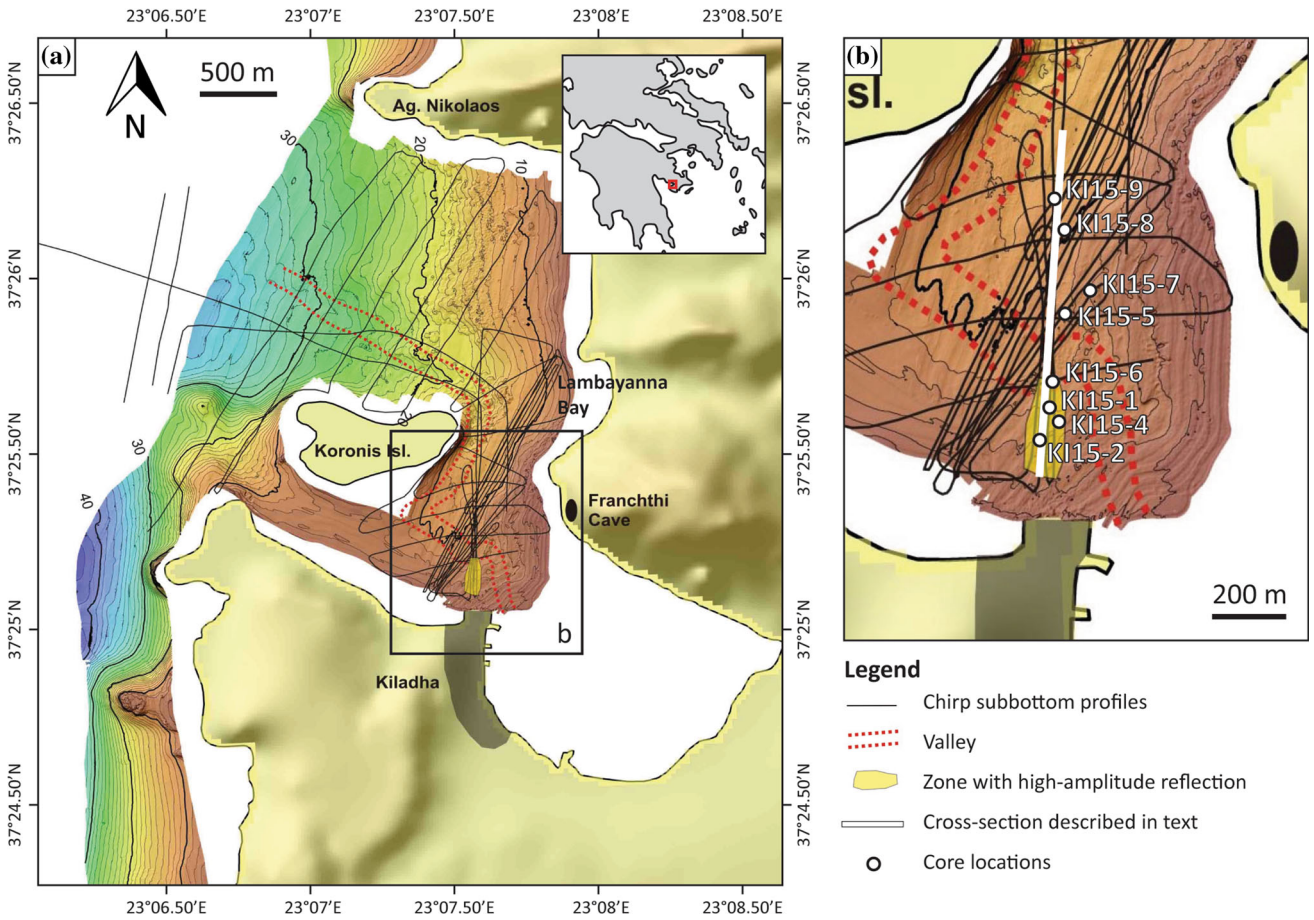

Fig. 2 **a** Map of Kiladha Bay with bathymetry and seismic lines (modified after Sakellariou et al. 2015); **b** Zoom showing core locations and seismic line (white) displayed in Figs. 3 and 6

Bronze Age settlement (~ 5000 year BP) in Lambayanna Bay, ~ 600 m northwards of Franchthi Cave (Beck and Koutsoumba 2015, 2016, 2017). These results motivated the retrieval of sediment cores in Kiladha Bay, with the following goals:

- Correlating the seismic stratigraphy with sediment cores.
- Documenting changes in the coastal sedimentary system through time.
- Understanding how and when the Holocene marine transgression occurred in Kiladha Bay.
- Contributing to a better understanding of how humans interacted with such landscape changes.

2 Study site

Kiladha Bay in the Aegean Sea is located in the southern Argolid, Peloponnesus, Greece (Fig. 1). It lies on the eastern side of the Argolic Gulf and is bordered by the present village of Kiladha at the south, Koronis Island at the west and Franchthi Cave at the north (Figs. 1, 2). The bay, ~ 1.5 km^2 large and up to ~ 14 m deep, has two exits to the deeper gulf. Local bedrock consists mainly of Mesozoic shallow-water limestone, which is extensively karstified in the region (Franchthi Cave, freshwater springs; Vitaliano 1987; van Andel 1987; Farrand 2000). The Aegean Sea is one of the most tectonically active regions in the Mediterranean, due to the combination of several tectonic processes, such as the westward migration of the Anatolian block and the subduction of the Eastern Mediterranean lithosphere under the Hellenic Arc, leading to extension in Central Greece and volcanic activity along the Hellenic Volcanic Arc (Papadopoulos et al. 2014; Sakellariou and Galanidou 2015 and references therein). The large rockfall inside Franchthi Cave could, for instance, have been caused by an earthquake in the area. The region around Kiladha is characterised by NW–SE, mostly active faults, causing uplifting and subsiding areas (Fig. 1; Sakellariou et al. 2015; Sakellariou and Galanidou 2015). Kiladha Bay has been identified as a horst bordered by two reverse faults (van Andel 1987).

3 Methods

3.1 Geophysical methods and sediment-core recovery

During the 2014 Terra Submersa expedition (Sakellariou et al. 2015; Beck et al. 2017) Kiladha Bay was investigated with hydroacoustic methods including hull-mounted multibeam swath-bathymetry (RESON SeaBat 7125; 200/400 kHz) and single-channel chirp seismic subbottom profiling (Geoacoustics Ltd.; frequency 2–7 kHz). On the basis of the interpretation of the seismic profiles, eight sediment cores, up to 6.3 m long, were retrieved in August 2015 within Kiladha Bay, from a floating platform. Following recovery of the undisturbed water–sediment interface and surficial sediments using a gravity corer, percussion piston-coring (UWITEC Ltd.) was used to retrieve longer sediment cores reaching down into the hardgrounds. All cores were recovered in 6-cm-diameter PVC liners.

3.2 Petrophysical and sedimentological methods

In the laboratory, a GEOTEK Multi-Sensor Core Logger (MSCL) was used to measure the p-wave velocity (PWV), wet bulk density (WBD) and magnetic susceptibility (MS) with a 5-mm-interval on whole core rounds. WBD was determined with gamma-rays absorption emitted by a ^{137}Cs-source. For the MS, an alternating magnetic field of 0.565 kHz was emitted by a Bartington loop sensor. P-waves were measured with two ultrasonic transducers at 1 MHz. After longitudinal opening, the cores were photographed with the Sigma 105 mm/1:2.8 DG Macro EX line scan camera of the GEOTEK MSCL. X-ray computed tomography (CT) was then performed on the cores using a Siemens Somatom Definition AS 64 CT-scanner, scanning 0.6-mm-thick layers with an overlap of 0.2 mm, a voltage of 140 kV, an adaptive radiation exposure (CARE Dose) and a matrix size of 512 × 512 pixels. The CT scans were thereafter processed with the OsiriX Lite 8.0.2 software into Maximum Intensity Projection 3D images. A composite section was constructed for each coring site by means of visual correlation of lithological features and petrophysical data. A qualitative macroscopic and microscopic description of the sediments was made based on the split-core images, wet sieving, and smear slide analysis, in order to determine lithotypes and lithostratigraphic units. The grain-size analysis was performed macroscopically and microscopically on the basis of the smear slide examination under the optical microscope according to Wentworth (1922). The families of some of the shells were identified in a macropalentological analysis.

3.3 Carbon, nitrogen and sulphur analysis

Total carbon (TC), total organic carbon (TOC), total nitrogen (TN) and total sulphur (TS) were measured with a Carlo Erba EA 1108 elemental analyser (CNS analysis). Inorganic carbon was removed using 1 M HCl at 70 °C prior to TOC content determination. The measured concentration of TOC was then multiplied by a conversion factor of 2 (Pribyl 2010), in order to estimate the weight percentage of organic matter (wt% OM). Total inorganic carbon (TIC) was calculated as the difference between TC and TOC. The wt% of calcium carbonate was obtained by multiplication of the TIC based on $CaCO_3$ stoichiometry using the factor of 8.33. The remaining material that was neither OM, nor carbonate, was assumed to be siliciclastics. The C/N ratio was also calculated, using the value of TOC (wt%) divided by TN (wt%). This ratio is a proxy indicating the origin of the OM, as marine or lacustrine phytoplankton has a C/N ratio between 4 and 10, whereas vascular land plants have a ratio usually larger than 20 (Meyers 1997; Meyers and Teranes 2001). Water content was estimated along the cores by weighing samples before and after freeze-drying.

3.4 Scanning-X-ray fluorescence

Scanning-X-ray fluorescence (XRF) was performed with an ITRAX-XRF core scanner (Cox Ltd.) equipped with a Cr-tube set to 30 kV and 50 mA. Split core surfaces were scanned at 1-cm-resolution with an integration time of 50 s. Five elements (Fe, Ti, Ca, Cl, S), measured in core KI15-2 (except the last core section) and in the lowest section of core KI15-6, were considered in the reconstruction of the palaeoenvironmental evolution of Kiladha Bay.

In this shallow marine environment, Fe and Ti are used as indicators for detrital input (Karageorgis et al. 1997; Vogel et al. 2010; Kylander et al. 2013). Ca is an indicator for endogenic/biogenic calcium carbonate formed in the sea (Karageorgis et al. 1997; Vogel et al. 2010), as well as for detrital calcite delivered through river input. Owing to the enrichment of Cl^- and SO_4^{2-} ions in seawater relative to freshwater, we employ Cl and S intensities as indicators for porewater salinities, with higher intensities being indicative for higher salinities and prevalence of sea- over freshwater (Tjallingii et al. 2007). Therefore, to avoid dilution effects caused by fluctuating concentrations of OM along the cores, we normalised the above-mentioned elements with Ti as conservative element (Löwemark et al. 2011). Thus, Ca/Ti and Fe/Ti ratios were also considered. The Ca/Ti ratio is an indicator for the input of endogenic/biogenic calcium carbonate relative to detrital sediment

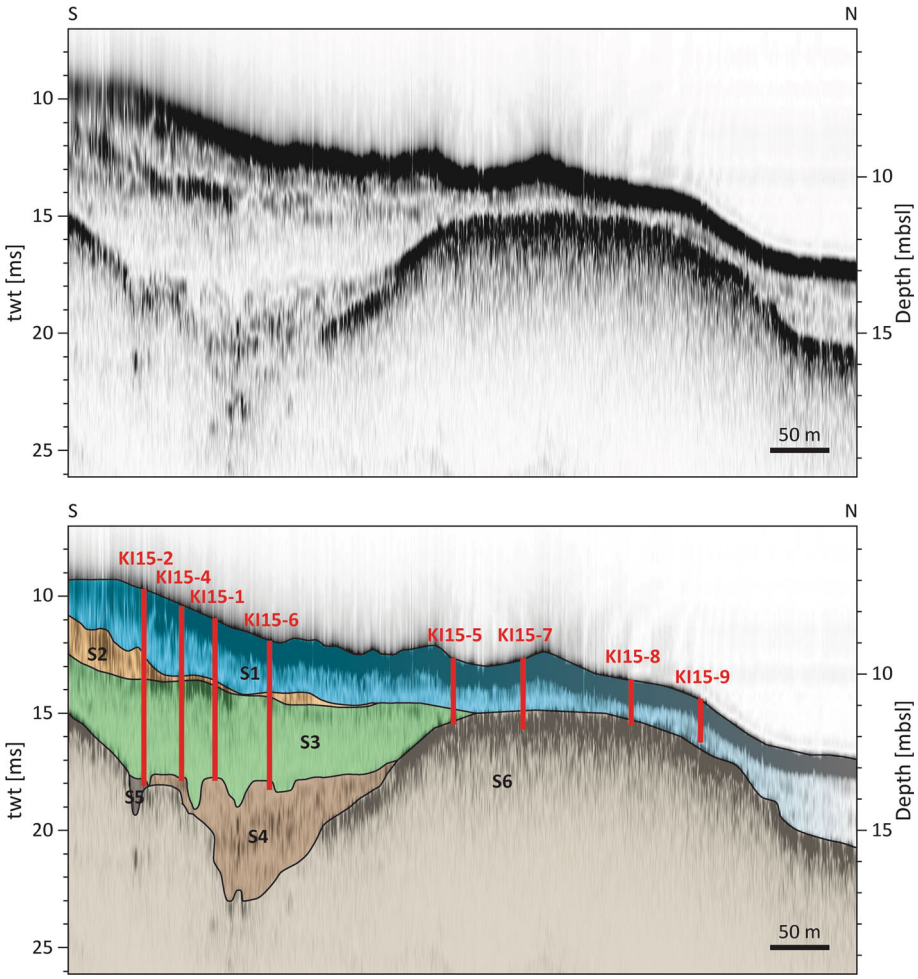

Fig. 3 Top: Seismic profile (white line on Fig. 2; modified after Sakellariou et al. 2015); bottom: Seismic profile displaying seismic units, as well as locations and lengths of cores. Vertical exaggeration = ×26. Depth in two-way traveltime (twt) (ms) on the left and in metres below sea level (mbsl) on the right (assumed Vp of water and sediment = 1500 m/s)

(Kylander et al. 2013). Hence, this ratio allows for differentiating carbonates produced in situ (high values) and those derived from terrestrial sources (low values). The Fe/Ti ratio is an indicator for the impact of RedOx processes that can alter the Fe concentration after burial through, for example, reductive dissolution of Fe-oxides/oxyhydroxides (Croudace et al. 2006). A constant supply of both Fe and Ti over time would thus result in a constant Fe/Ti ratio. Deviations from this constant ratio towards lower values indicate reductive dissolution of Fe and deviations towards higher ratios indicate either oxidative deposition of Fe from porewaters at the RedOx front or enrichment of Fe due to precipitation in form of Fe-sulphides.

3.5 ^{14}C-dating

Six samples of organic remains (two seeds, a leave and three other plant macrofossils) were dated with the accelerator mass spectrometer (AMS) of the Laboratory for the Analysis of Radiocarbon with AMS (LARA) of the University of Bern. The results were calibrated and an age-depth model was produced using the Bayesian age-depth modelling software Bacon 2.2 (Blaauw and Christen 2011) and the IntCal13 calibration curve (Reimer et al. 2013).

4 Results

4.1 Bathymetry, seismic profiles and core locations

The bathymetry data of Kiladha Bay (Fig. 2) reveals a shallow and very flat pass (~ 8 m deep) to the south of Koronis Island, opening westward to the Argolic Gulf, where water depth suddenly increases. Another pass, wider and with a regular seaward slope of ~ 1°, leads from Kiladha Bay to the Argolic Gulf, going northward between Koronis Island and Franchthi Cave. Six seismic stratigraphic units were determined, based on seismic facies and unconformities (Fig. 3; Sakellariou et al. 2015). As a convention, the tops of the chirp-reflections were used as the limits between successive units. The top of lowermost seismic unit (*S6*) is characterised by its high-amplitude reflection, forming towards the north a terrace at ~ 11 m

Table 1 Shotpoints on seismic lines from Sakellariou et al. (2015), coordinates, approximate water depths and composite core lengths (metre composite depth, mcd) for each coring site

Site	Shotpoint on seismic line	Latitude (°)	Longitude (°)	Water depth (m)	Composite core length (mcd)
KI15-1	400/Line 113115	37°25′10.72″	23°07′34.00″	8.6	~ 5.2
KI15-2	200/Line 113115	37°25′08.86″	23°7′33.14″	7.6	6.311
KI15-4	638/Line 105045	37°25′10.09″	23°07′34.62″	7.7	~ 5.6
KI15-5	800/Line 104517	37°25′16.72″	23°07′35.35″	9.1	2.124
KI15-6	950/Line 105045	37°25′12.33″	23°07′34.71″	9.2	4.767
KI15-7	1700/Line 110619	37°25′18.09″	23°07′37.19″	8.6	2.307
KI15-8	3750/Line 093227	37°25′22.05″	23°07′35.65″	10.3	1.467
KI15-9	2111/Line 085402	37°25′24.06″	23°07′35.42″	11.2	~ 1.4

Table 2 Lithotypes from Kiladha Bay: macroscopic description, wet bulk density (WBD), magnetic susceptibility (MS), wt% water, wt% calcium carbonate ($CaCO_3$), wt% organic matter (OM), wt% siliciclastics (Silic) and total organic carbon/total nitrogen (C/N) ratio

Lithotype	Description	WBD (g/c^3)	MS (10^{-5} SI)	Water (wt%)	$CaCO_3$ (wt%)	OM (wt%)	Silic (wt%)	C/N
A	Grey to reddish-brown sandy silt with clay, faintly laminated, many intact and fragmented marine shells, some rounded pebbles (ø ≤ 4 cm), some organic remains	1.5–2.0	2–11	34–49	39–62	3–6	36–57	8–11
B	Beige, homogeneous clayey silt with sand, some intact and fragmented marine shells, very few gravels	1.5–1.8	1–5	32–49	37–56	3–5	42–59	10–13
C1	Beige, sandy silt with clay, many intact and fragmented marine shells, very few gravels	1.6–1.9	1–3	30–47	43–58	2–3	48–54	10–13
C2	Beige, sandy silt with clay, many intact and fragmented marine shells, lot of gravel (≤ 1 cm)	1.8–1.9	3–4	32–36	48–54	~ 3	43–49	12–13
C3	Beige, sandy silt with clay, shell-supported, few gravel (≤ 5 mm)	1.8–2.0	0–2	28–34	43–55	2–3	41–55	15–20
D1	Blue-grey with black stains, well-sorted silty clay, plant remains, few charcoal pieces, very few shells	1.7–1.8	3–7	32–35	26–30	1–2	69–73	16–19
D2	Grey, sandy silt with clay, few shells, some gravels, some charcoal pieces, some organic remains	1.8–2.0	9–12	27–30	29–34	1–2	64–70	19–27
E1	Reddish-brown with black stains, well-sorted, stiff clay, very few (marine and brackish/freshwater) shells, very few organic remains	1.7–1.8	12–178	29–36	21–35	1–2	64–78	13–19
E2	Reddish-brown with black stains, stiff clay with coarse sand grains, organic remains, charcoal pieces, very few (marine and brackish/freshwater) shells	1.7–1.9	135–195	28–34	17–26	~ 1	75–81	11–15
F1	Greyish-brown with black stains, very well-sorted, very stiff clay, organic remains, very few shells	1.7–1.9	109–161	25–30	20–24	1–2	75–79	13–15
F2	Greyish-brown with black stains, very well-sorted, very stiff clay, few sand, very few organic remains, very few shells	1.9–2.1	130–159	21–22	26–28	~ 1	71–73	11–14
F3	Greyish-brown with black stains, very well-sorted, very stiff clay, lot of coarse sand (≤ 1 mm), some gravel (≤ 1 cm), very few shells	~ 2	130–142	~ 19	~ 29	< 1	70	16
G	Chocolate-brown with black stains, stiff, silty clay with sand, many rocks (≤ 6 cm), lot of gravel, organic remains, very few (marine and terrestrial) shells	1.9–2.4	87–196	23–26	11–23	1–2	76–87	13–19
H	Beige, silty sand, carbonate rubble, some angular rocks, few charcoal pieces, very few shells, very few bone fragments, pottery sherds	1.8–2.4	4–56	–	–	–	–	–

below sea level (mbsl). The top of *S6* deepens gradually southwards down to ~ 17.5 mbsl and then rises again, forming a ~ 6.5-m-deep and ~ 300 m wide valley with lateral slopes that are slightly dipping with ~ 2°. The reflection at the bottom of this valley, between ~ 15.5 and 17.5 mbsl, is irregular with no sharp boundaries. The trajectory of the valley, as interpreted on the basis of the numerous seismic profiles obtained during the Terra Submersa expedition, can be visualised on the bathymetric map (red-dotted lines on Fig. 2). A ~ 20-m-large hole or trench appears on the southern edge of the valley, at a depth of ~ 13.5 to 15 mbsl. It is filled by a unit with chaotic seismic facies (*S5*). Two seismic units were defined inside the valley: *S4* and *S3*. Both reach maximum thicknesses of up to 4 m. The lower one (*S4*) fills the valley from its bottom up to ~ 13.5 mbsl. It displays an irregular seismic facies of medium-amplitude reflections with weak layering. Its subhorizontal top is incised by channel-like features. The overlying unit *S3* appears transparent and fills the valley up to the terrace formed by *S6*. The top of unit *S3*, between 9.5 and 11 mbsl, is formed by a reflection with a laterally changing amplitude. This reflection can be traced from the southern edge of the seismic profile to its onlap onto the top of the terrace in the north. The reflection has a particularly high amplitude near the southern part of the cross-section, which is located in a limited area, highlighted in yellow in Fig. 2 (Sakellariou et al. 2015). Overlying unit *S2* occurs in up to 1 m thick lense-shaped bodies, as it is laterally non continuous. Uppermost seismic unit *S1*, capped by the current sea floor, overlies locally *S2* lenses (where present), *S3* and, on the northern terrace, *S6*. It has a thickness between 1.5 and 2.5 m and does not display internal structures.

The locations of the cores (Figs. 2, 3 and Table 1) were chosen as to recover all major seismic units. The four longest cores (KI15-1, -2, -4 and -6) penetrate seismic units *S1* to *S3*. Cores KI15-1, -2 and -4 penetrate the top of *S3* where it is characterised by a high-amplitude reflection and where *S2* is thin or absent. The bottom of KI15-2 reaches *S5*, whereas those of KI15-1, -4 and -6 reach *S4*. KI15-5 contains seismic units *S1* and *S3*, as well as possibly the top sediments of *S6* along the slope of the valley. Cores KI15-7 and -8 penetrate *S1* and reach the top of *S6*. Core KI15-9 only enters seismic unit *S1*. As cores KI15-1 and -4 penetrate the same seismic units than core KI15-6, but recover

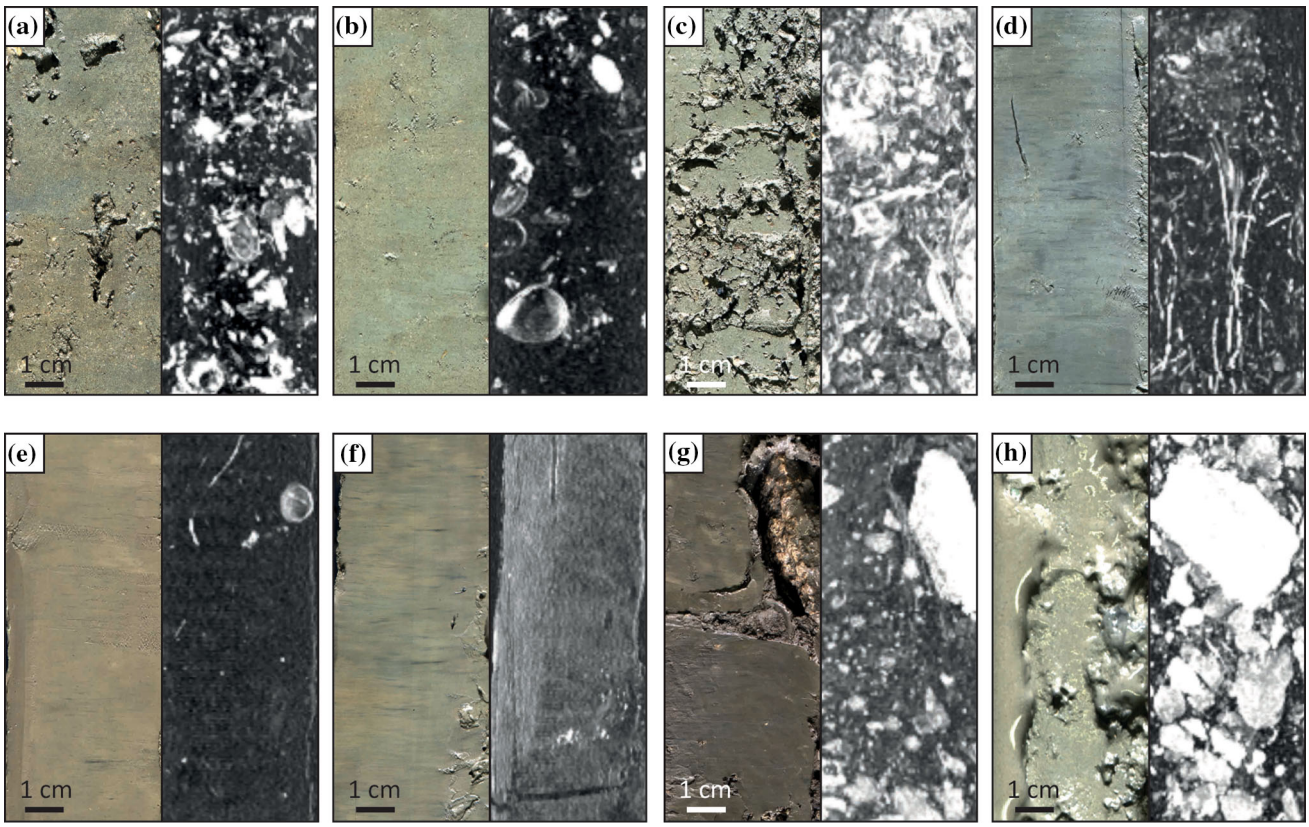

Fig. 4 Line scan and CT-images of lithotypes (composite depth of images indicated in parentheses): **a** Lithotype A (KI15-2, 11–21 cmcd); **b** Lithotype B (KI15-2, 125–135 cmcd); **c** Lithotype C3 (KI15-2, 276–286 cmcd); **d** Lithotype D1 (KI15-2, 320–330 cmcd); **e** Lithotype E1 (KI15-2, 464–474 cmcd); **f** Lithotype F2 (KI15-6, 457–467 cmcd); **g** Lithotype G (KI15-2, 585-595 cmcd); **h** Lithotype H (KI15-7, 181–191 cmcd)

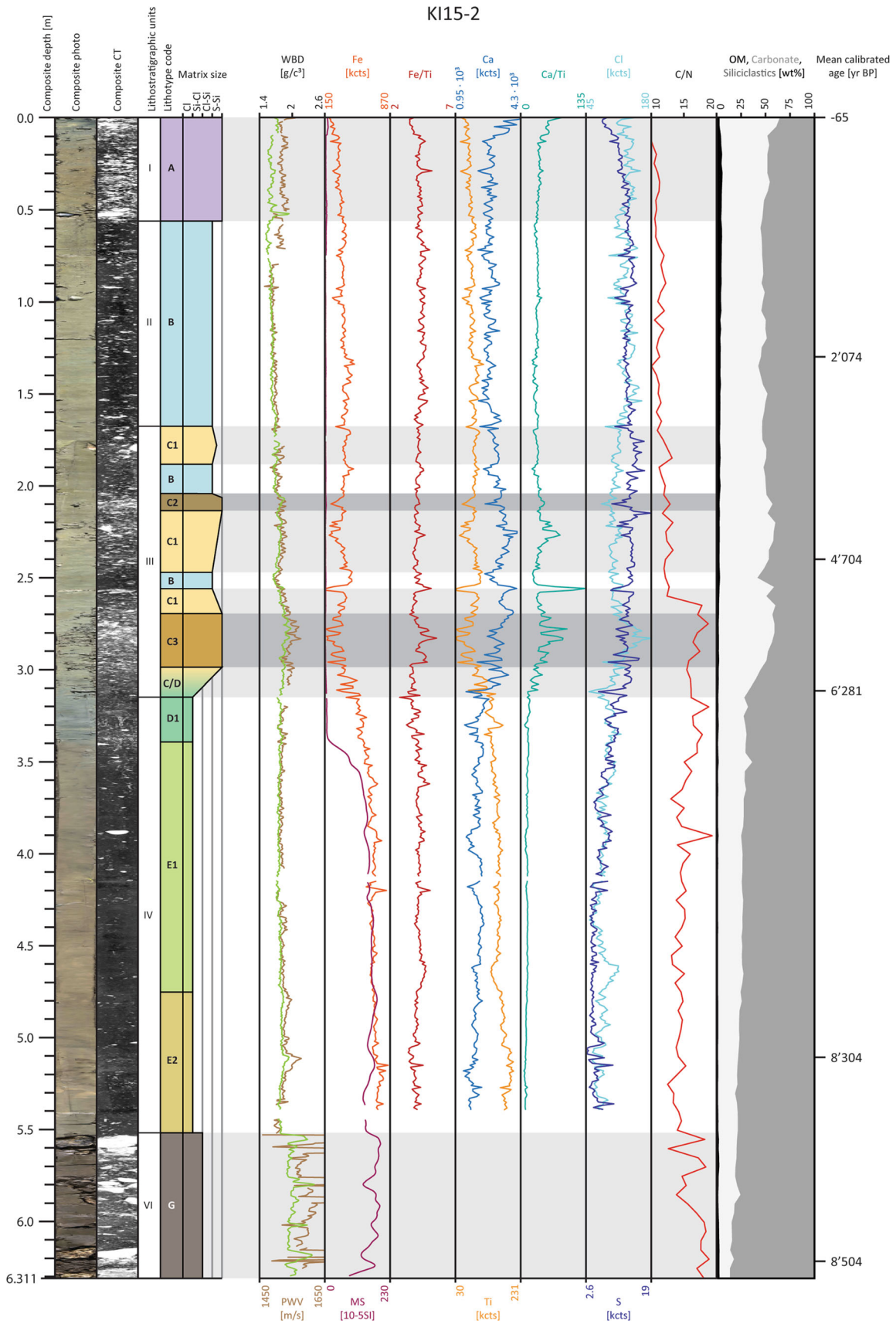
KI15-2
Composite depth [m]
Composite photo
Composite CT
Lithostratigraphic units
Lithotype code
Matrix size
Cl
Si-Cl
Cl-Si
S-Si
WBD [g/cm³]
Fe [kcts]
Fe/Ti
Ca [kcts]
Ca/Ti
Cl [kcts]
C/N
OM, Carbonate, Siliciclastics [wt%]
Mean calibrated age [yr BP]
I
II
III
IV
VI
A
B
C1
B
C2
C1
B
C1
C3
C/D
D1
E1
E2
G
0.0
0.5
1.0
1.5
2.0
2.5
3.0
3.5
4.0
4.5
5.0
5.5
6.0
6.311
-65
2'074
4'704
6'281
8'304
8'504
PWV [m/s]
MS [10-5SI]
Ti [kcts]
S [kcts]

◀**Fig. 5** Composite section of core KI15-2 showing (from left to right) core line scans, computed tomography (CT)-image, lithostratigraphic units, lithotypes, grain size pattern of the matrix (Cl = clay; Si–Cl = silty-clay; Cl–Si = clayey-silt; S–Si = sandy silt), wet bulk density (WBD), p-wave velocity (PWV), magnetic susceptibility (MS), element intensities for Fe, Ca, Ti, Cl and S quoted as kilocounts, ratios of Fe/Ti and Ca/Ti, C/N ratio, percentages of organic matter (OM), carbonate and siliciclastics, and AMS ^{14}C-ages

less sediment from *S4*, they were not investigated, neither was core KI15-9.

4.2 Results of sediment-core analyses

Using the results obtained by the macro- and microscopic sediment description as well as the petrophysical (CT, WBD, MS) and CNS analyses, eight lithotypes with some sub-types were defined, which are described in Table 2 and shown with core images and respective CT-scans in Fig. 4. The composite section of core KI15-2 was the longest and most complete amongst the cores so that its detailed analyses are described and interpreted in great detail (Fig. 5).

4.2.1 Lithostratigraphic units and seismic-to core correlation

The succession composed of eight lithotypes was divided into seven lithostratigraphic units (VII-I) marking major changes in the palaeoenvironment (Fig. 5). The seismic-to-core correlation of core KI15-2 (Fig. 6) relates these lithostratigraphic units to the seismic units (*S1*–*S6*) based on changes in PWV and WBD (Fig. 5).

Lowermost *Unit VII*, solely composed of lithotype H (Fig. 4h) and the equivalent of *S6*, occurs in cores KI15-5, -7 and -8 and is characterised by the presence of many rock pieces, few bone fragments, few charcoal pieces, and two pottery sherds. Overlying *Unit VI*, correlating to *S5*, consists of lithotype G (Fig. 4g) and has been exclusively recovered in core KI15-2 (Figs. 5, 6). The massive chocolate-brown sediments of this unit contain large clasts of carbonate rubble and very few marine (e.g. Cerithiidae) and terrestrial (e.g. Ferussaciidae) shells. *Unit V* (lithotypes E1, F1, F2 and F3, coinciding to *S4*; Fig. 4f) is only present in core KI15-6 and is composed of mottled greyish-brown, stiff clay sediments with rare marine (Cardiidae, Rissoidae) and freshwater or brackish shell fragments (e.g. Hydrobiidae). The basal 5 cm are enriched in coarse sand. This unit displays an upcore increase in Fe and Ti contents, decreasing Ca-carbonate content, and a low Ca/Ti ratio. *Unit IV* (lithotypes D1, D2, E1 and E2, coinciding with *S3*; Fig. 4e) overlies *Units VII* (in core KI15-5), *VI* (in core KI15-2) and *V* (in core KI15-6). The transitions with underlying *Units VII* and *VI* are sharp, and marked by a colour change from beige, respectively chocolate-brown, to reddish-brown and the sudden upcore disappearance of large pebbles (Figs. 4e, 5). On the contrary, the transition from *Unit V* to *Unit IV* is very gradual and defined at the gradual upcore decrease of sediment density and stiffness. Traces of bioturbation were found in *Unit IV*, together with few shells identified as marine species typical for a subtidal zone, close to a shore (Cardiidae, Cerithiidae, Pyramidellidae, Rissoidae, Triphoridae, Veneridae, etc.). It also shows high Fe and Ti contents and low Ca, Cl and S contents, and a low Ca/Ti ratio (Fig. 5). The top ~ 15 to 30 cm sediment sequence of this unit (lithotype D1 in cores

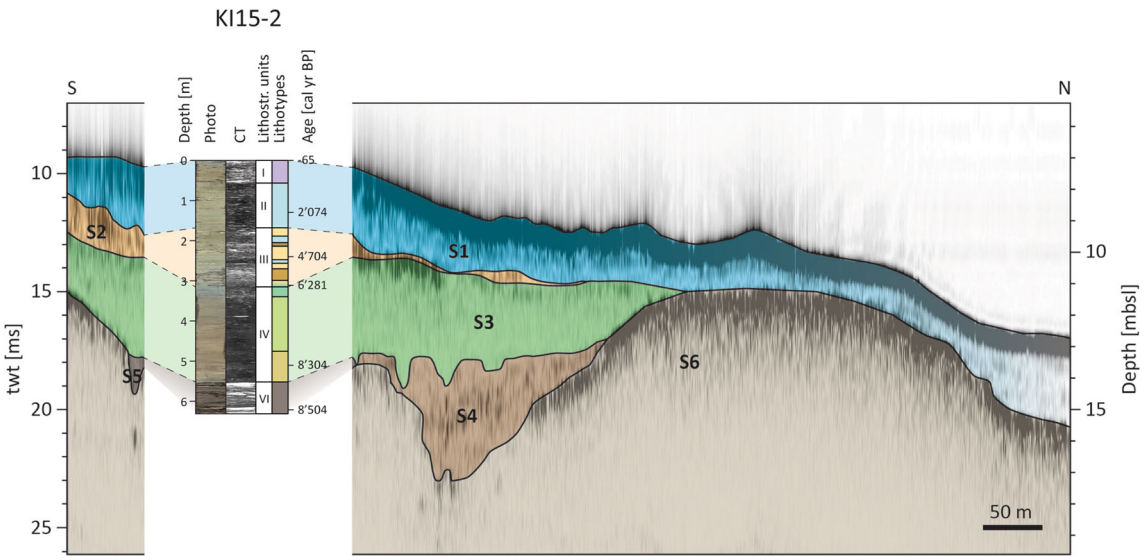

Fig. 6 Correlation of core KI15-2 within seismic profile (white line on Fig. 2; modified after Sakellariou et al. 2015)

Table 3 Results of AMS ^{14}C-dating

BE nr.	Core section	Section depth (cm)	Composite depth (cmcd)	Material	AMS ^{14}C age (year BP)	± 1σ (year)	Calibrated age (year BP, 2σ)	Mean (year BP)	δ^{13}C (‰)
5942.1.1	KI15-2-2b	55.5–56.5	130.1–131.1	Grape seed	2103	19	2132–2003	2074	− 28.6
6061.1.1	KI15-2-4a	53.2–54.2	510.1–511.1	Leave	7496	50	8391–8197	8304	− 27.6
6062.1.1	KI15-6-3c	50.5–51.5	427.7–428.7	Plant macrofossil	7451	23	8342–8198	8269	− 26.4
6397.1.1	KI15-2-2c	65.5–70.5	239.0-244.0	Plant macrofossil	4152	19	4823–4585	4704	− 13.9
6398.1.1	KI15-2-3a	78.1–82.8	310.0–314.7	Plant macrofossil	5482	44	6396–6201	6281	− 9.9
6399.1.1	KI15-2-4b	80.5–85.5	619.7–624.7	Seed	7731	22	8579–8435	8504	− 23.9

The age calibrated with IntCal13 is given with a 2σ-time span (95.4%); the last column shows the measured δ^{13}C, which gives indications about the origin of the material

KI15-2 and -6; lithotype D2 in core KI15-5) displays a colour change from reddish-brown to blue-grey (Figs. 4d, 5), together with a strong MS decrease and a very slight decrease in the Fe content and the Fe/Ti ratio, accompanied by an increase of S and Cl contents (340-316 cm composite depth (cmcd) in core KI15-2; Fig. 5). It contains plant remains, possibly roots, which appear denser than the surrounding sediments on the CT-images, possibly indicating carbonate mineralisation (Fig. 4d). Changes in sediment-colour, increases in shell and carbonate contents, and decreases in MS and siliciclastics contents mark the transition from *Unit IV* to *Unit III* in cores KI15-2, -5 and -6 (Fig. 5), whereas a more gradual transition can be observed from *Unit VII* to *Unit III* in cores KI15-7 and -8. *Unit III* is composed of poorly-sorted beige sediments (lithotypes B, C1, C2 and C3) and is very rich in bioclastic debris (Fig. 4c) of the same marine fauna as in *Unit IV*. It correlates to *S2*. In core KI15-2, shell concentration decreases at 256-247 and at 204-188 cmcd, represented by lithotype B (Fig. 5). A slight decrease of shell concentration further occurs between sub-types C1 and C3 in core KI15-6 at 147-138 cmcd. Very few (< 2%) volcanic glass shards were found in lithotype C1 (KI15-2, 188 cmcd) and C2 (KI15-2, 208 cmcd). XRF-results fluctuate relatively strongly in *Unit III*, yet the overall trend displays lower Fe and Ti content and higher Ca, Cl and S contents than in the downlying units (Fig. 5). The transition to overlying *Unit II* (lithotype B, Fig. 4b) is marked by a gradual decrease in shell content, again of the same marine species as in Units *IV* and *III*. This unit displays Ca/Ti ratio and Ca, Cl and S contents that are higher than in *Unit IV* and below, and lower Fe and Ti contents (Fig. 5). Topmost *Unit I* entirely consists of faintly laminated lithotype A (Fig. 4a). It is characterised by a surprisingly high pebble and shell concentration, as well as greyish top sediments. The shells consist of a similar marine fauna as in *Units IV* and *III* and *II*. Fe/Ti ratio decreases towards the top of core KI15-2 (12-0 cmcd), together with Fe, Ti, Cl and S contents, whereas Ca content and Ca/Ti ratio increase (Fig. 5). Lithostratigraphic *Units I* and *II* together correlate to *S1*.

4.3 Results of AMS ^{14}C-dating and age model

AMS ^{14}C-dating was performed on five samples from core KI15-2 and one sample from core KI15-6 (Table 3). Four of the samples have a δ^{13}C value between − 23 and − 29‰, indicating that they are probably C3 land plants (Meyers 1997). However, the δ^{13}C of two samples (6397.1.1 and 6398.1.1) is much higher than in the other samples, suggesting aquatic plants (Stuiver and Polach 1977; Carlier ET AL. 2009). For this reason, imprecisions due to reservoir effect may be considered for both samples.

The age model (Fig. 7) shows a consistent age-depth correlation back to ~ 8500 cal year BP. Estimated sedimentation rates vary between 0.5 and 4.2 mm/year (Fig. 7). A hiatus was inferred at 320 cmcd based on the presumably exposure lithologies.

5 Discussion

5.1 Reconstruction of the palaeoenvironmental evolution

The lithostratigraphic units are here interpreted in terms of environmental evolution, from the LGM to the present. Time frame is based on the age-model (Fig. 7). This reconstruction is illustrated by a sketch (Fig. 8).

5.1.1 Unit VII (~ S6): Top of the Pleistocene exposure horizon

The lowermost unit consists of the top of the Late Pleistocene palaeolandscape that was exposed during the LGM, Late Glacial and Early Holocene. A river valley incises this landscape, channelling the runoff waters to the palaeoshore

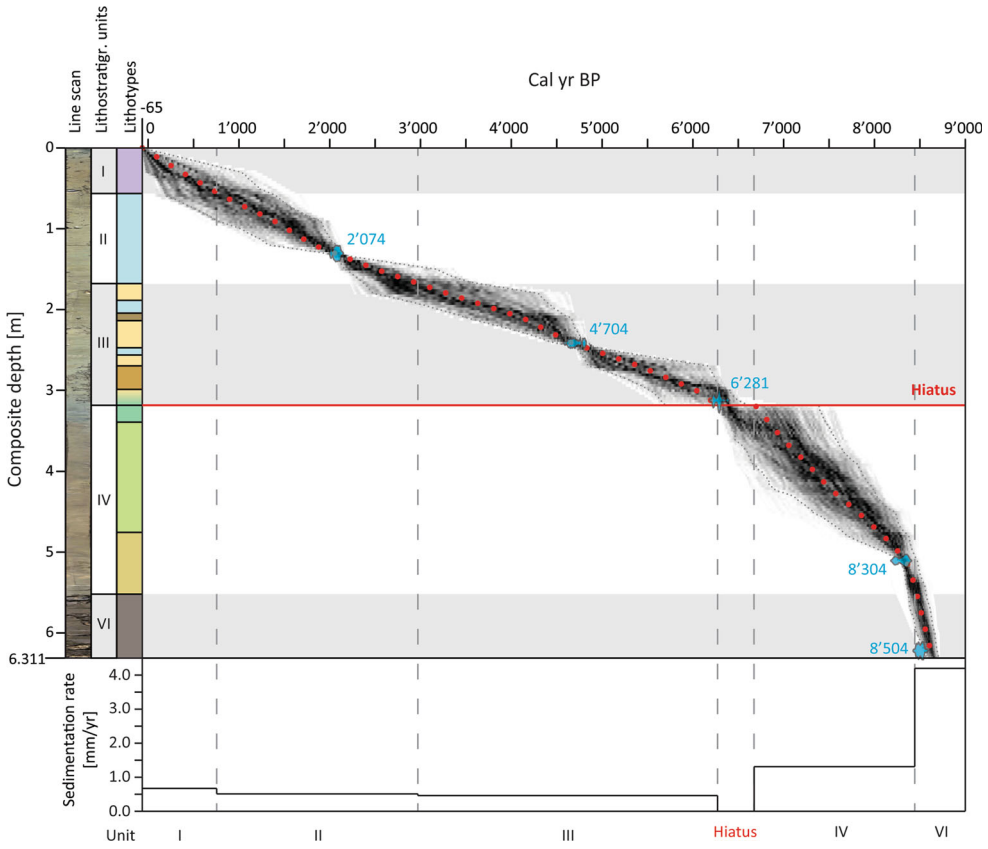

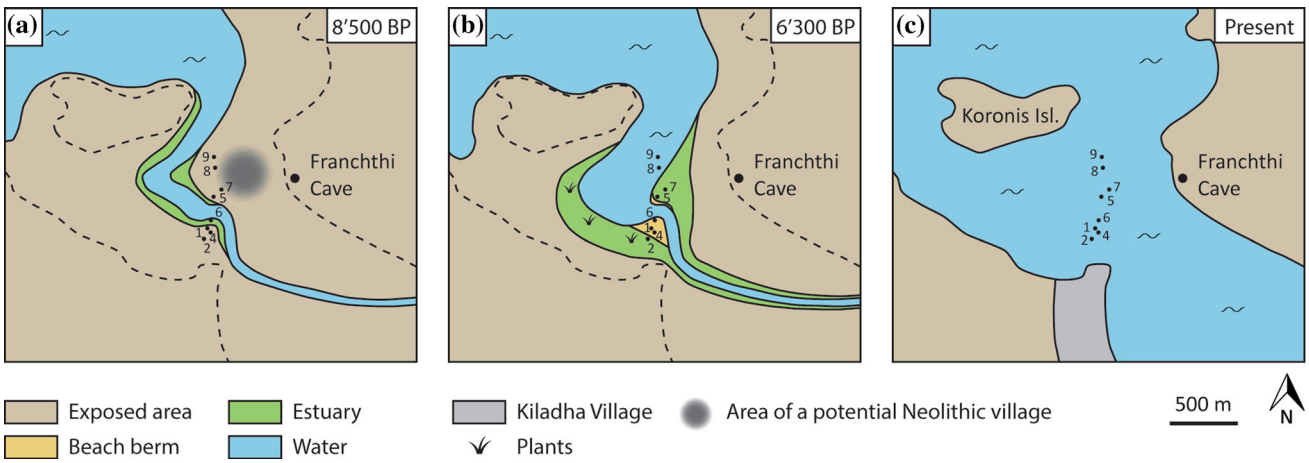

Fig. 7 Age-depth model and sedimentation rate for core KI15-2. The calibrated ^{14}C ages are displayed in blue, the greyscale curve shows the probability of the interpolated ages (the darker part has the higher probability) and the red dotted curve shows the weighted mean age for each depth

Fig. 8 Reconstruction of the landscape evolution in Kiladha Bay with coring locations; **a** 8500 cal year BP; **b** 6300 cal year BP; **c** Present state

in the west. Large limestone and few crystalline rock pebbles occur, indicating exposure of this surface.

5.1.2 Unit VI (~ S5): flooding/weathering processes, prior to ~ 8500 cal year BP

The ~ 20-m-diameter hole or trench cutting through the southern edge of the river valley is filled with rubble and gravels of various lithologies (mostly limestone, also some radiolarites) in a fine-grained chocolate-brown matrix with remains of terrestrial plants. These characteristics indicate that this unit was deposited in a terrestrial setting with prevailing fluvial processes and soil formation. The presence of few marine shells within an otherwise terrestrial macrofauna suggests that the sediments of *Unit VI* may have derived from the nearby sea and were deposited on land by storm surges or wave action, as supported by the relatively high sedimentation rate of this unit (Fig. 7).

5.1.3 Unit V (~ S4): river valley filled with flood deposits, prior to ~ 8500 cal year BP

The valley is filled with lithostratigraphic *Unit V* up to a level of ~ 13.5 mbsl. Only the top 80 cm of this unit was recovered in core KI15-6. The stiff clay lithology with coarse sand (basal 5 cm) is marked by high WBD, together with high MS values and high Fe, Ti and siliciclastics contents, and indicates a predominantly terrestrial origin of the sediments. This lithology and the seismic geometries point towards a fluvial depositional environment in an active river valley in which flooding was more prevalent during the Early Holocene compared to today. This is supported by several other studies from the region, which also indicate a wetter Early Holocene (e.g. Ariztegui et al. 2000).

5.1.4 Unit IV (~ S3): estuary embayment, ~ 8500 to ~ 6300 cal year BP

Overlying *Unit IV* displays very similar lithological and geochemical properties as *Unit V*. It suggests that the material deposited between 8500 and 6300 cal year BP comes from a similar source as before, yet is marked by lower density and stiffness and a higher water content. This change may be related to the rising sea level, likely causing a groundwater-table rise (Rotzoll and Fletcher 2013), which eventually transforms the river valley characterised by repeated flooding into a permanently flooded estuary. These fine-grained detrital sediments accumulated up to the level of the terrace, on which they onlap (Figs. 3, 6). When the accommodation space of the valley was filled, the depositional area widened consequently as water was not anymore confined to the river valley and could spread on the newly created flood plain below Franchthi Cave, creating paralic swamps (Vött 2007) with their characteristic vegetation cover. Due to stagnating water, reducing conditions occurred up until the soil surface, leading to reductive dissolution of Fe-oxides and formation of Fe-sulphides, with the result that sediment colour changed from reddish-brown to blue-grey. In the same sediment sequence, a strong decrease in MS occurs, supporting the inferred change in Fe mineralogy, from Fe-oxides to Fe-sulphides (Dearing 1999; Sandgren and Snowball 2001). In addition, the Fe/Ti ratio is slightly lower within the grey-blue sequence, which also indicates loss of Fe as a result of reductive dissolution (Croudace et al. 2006).

5.1.5 Unit III (~ S2): shore deposits/Marine transgression, ~ 6300 to ~ 3000 cal year BP

The lithotypes C1-D1 in *Unit III*, with abundant marine shells, witness that marine conditions were progressively installed around 6300 cal year BP. During this time span, siliciclastics content diminishes from ~ 70 to < 50 wt%, while carbonate content increases from ~ 30 to > 50 wt%. Simultaneously, Ca, Cl and S signals increase gradually, and Fe, Ti and MS display a diminishing signal. All these proxies indicate that around 6300 cal year BP, the rising sea level submerged a part of Kiladha Bay, first near location of cores KI15-9, -8 and -6, then broadening to locations of cores KI15-1, -2, -4, -5, -7. It eroded parts of the underlying *Unit IV*, causing a ~ 400 year hiatus in the stratigraphy, from ~ 6700 to ~ 6300 cal year BP. The shell-dominated fabrics with marine gastropods and bivalves represent dislocated littoral materials forming a beach at the shoreline between Franchthi Cave and Koronis Island. Such shell-rich sediments were deposited over apparently more than 3000 years, from ~ 6300 to 3000 cal year BP, which to some degree might be an overestimation due to the less accurate age model for this period (Fig. 7). An accumulation of ~ 1 m of shells occurs in core KI15-2 with three alternations between shell-poor sediment (lithotype B) and pulses of coarse shells (lithotypes C1, C2, C3). Very few (< 2%) volcanic glass shards were found in the top of this unit. According to the age-depth model, this could be linked to the ~ 3600 cal year BP Santorini eruption (1627–1600 BC, 95% confidence, Friedrich et al. 2006). This eruption, as well as other tectonic processes, is known to have triggered tsunamis in the Eastern part of the Mediterranean (e.g. Minoura et al. 2000; Bruins et al. 2009; Papadopoulos et al. 2014; Ntageretzis et al. 2015a, b), contributing to the accumulation of coarse shells at the shorelines. We cannot rule out the possibility that some of the coarser layers that we found in Unit III have been deposited by tsunami waves, although our data are not sufficiently unambiguous to discern these.

In core KI15-2, the base of *Unit III* occurs at ~ 10.8 mbsl (~ 7.6 m water + 3.2 m of sediment depth). The depth of this palaeoshoreline marks approximately the elevation of sea level. This is consistent with van Andel (1987) and Lambeck (1996), who state that in the same area, sea level was at ~ 11 mbsl between 7610 ± 150 and 6220 ± 130 cal year BP. This depth, however, does not match the global sea-level curve (Lambeck et al. 2014) indicating a sea level around 3.1 mbsl at ~ 6300 cal year BP (Fig. 9).

5.1.6 Unit II (lower part of S1): shallow marine sediments, ~ 3000 to ~ 750 cal year BP

Sea level continued to rise, thus migrating the shoreline landward and burying the underlying shore deposits. Petrophysical and geochemical results of *Unit II* show very constant conditions, with a macrofauna typical for a

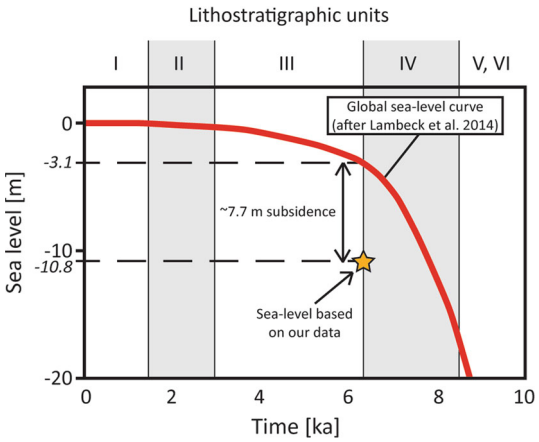

Fig. 9 Global averaged sea-level curve for the last 9000 year BP (modified after Lambeck et al. 2014) with lithostratigraphic units from Kiladha Bay

subtidal zone in a few metres depth close to the shore. The high carbonate, Ca, Cl and S contents, high Ca/Ti ratio and low siliciclastics, Ti and Fe contents confirm the shallow marine environment.

5.1.7 Unit I (upper part of S1): contemporary eutrophicated marine sediments, ~ 750 cal year BP to the present

The topmost unit shows in all the cores a strong enrichment in shells and pebbles. The thickness of this unit decreases from southernmost core KI15-2 (~ 55 cm) to northernmost cores KI15-7 and -8 (~ 12 to 14 cm). As all sites are currently 0.2–0.4 km offshore in ~ 8 m of water, these large clasts appear exotic in the fine-grained background deposits and are not easy to explain. We propose that the pebbles are related to human activity and could have been dropped during construction works on Koronis Island requiring many boat trips with building material back and forward across the bay. The high concentration of shells, which might be in situ, may be caused by eutrophication as since the second half of the 20th century, human activity caused a strong increase in nutrients such as N and P coming from agriculture into the sea (Gooday et al. 2009). The impact of these nutrients, enhancing algal and faunal growth and causing oxygen depletion, is also reflected by the greyish layers with a decreasing Fe/Ti ratio, indicating reducing conditions (Croudace et al. 2006) at the top of the sediment sequence from Kiladha Bay. The mean value of the age-depth model situates this sequence from ~ 750 cal year BP to the present. However, as eutrophication intensified quite recently, it would be more likely that this unit was deposited during the last century only. Bioturbation and sinking-in of dropping pebbles may have blurred the transition and caused an older apparent age.

This palaeoenvironmental reconstruction reflects the highly dynamic interplay between sea-level changes induced by eustatic and local effects and coastal depositional processes (e.g. van Andel and Lianos 1983; Lambeck 1996; Vött 2007; Mourtzas and Kolaiti 2013; Pavlopoulos et al. 2013; Weiberg et al. 2016; Avramidis et al. 2017). As discussed above, the reconstructed sea level does not match the global sea-level curve, indicating significant subsidence due to tectonic processes in the eastern Argolic Gulf. According to the shoreline interpretation of the marine transgressional unit at the base of *Unit III*, relative sea level can be determined for this time of 6300 year BP at 10.8 m below current sea level (Fig. 9). As the global sea level was ~ 3.1 m below today's sea level at that time, we can estimate a relative subsidence of ~ 7.7 m explaining the offset of the regional to the global sea-level curve (Fig. 9).

In addition, several archaeological sites (Halieis, Dardiza, Salanti, Lambayanna) of different ages have been discovered in the broad area around Kiladha Bay, submerged at various depths ranging from 1 to 3 m below present sea level. Although it is not known what was the exact position of the palaeoshorelines close to each one of the submerged sites, it is evident that subsidence was not uniform throughout this area. This is in agreement with the presence of active faults mapped offshore by Sakellariou et al. (2015), crosscutting this area in several tectonic blocks with distinct vertical tectonics history.

5.2 Archaeological implications and significance

The reconstruction of the palaeolandscape evolution in Kiladha Bay from ~ 8500 cal year BP to the present can now be put in the context of human occupation of the area. In fact, a pottery sherd (Fig. 10), along with other possible archaeological artefacts, was retrieved from the bottom of core KI15-5, near the top of the glacial exposure horizon. This blackish potsherd with a surface slip and painted decoration has been assigned chronologically to the Early to Middle Neolithic period (~ 8000 year BP in Greece; Vitelli, pers. comm., 2015). Another poorly conserved pottery sherd was found at the bottom of core KI15-8, also within the exposure horizon. These findings show that humans were present in this dynamic landscape with a migrating coastline, although they do not indicate where their village was. Nevertheless, one can assume that people practising agriculture would build a village near a fertile environment, such as what is provided by a floodplain (Bonsall et al. 2002; Berger and Guilaine 2009; Weiberg et al. 2016). Moreover, the sediments from the floodplain (bottom of core KI15-6) may act as excellent raw material to produce pottery. For these reasons, we agree with van Andel (1987), who suggests that the terrace above the river valley could be an ideal location to build a Neolithic village (shaded area in Fig. 8a): this apparently safe ground

Fig. 10 Pottery sherd with a surface slip and painted decoration (Early to Middle Neolithic). Image: Bay of Kiladha project

would be close to the crop fields and to a source of raw material, yet somehow protected from floods. Furthermore, around 8000 cal year BP, the shore was located between Koronis Island and Franchthi Cave (Fig. 8a), offering a protected environment and a source of seafood. Last but not least, nearby karstic springs (van Andel et al. 1980) could provide a source of freshwater. From ~ 8500 to ~ 6300 cal year BP, the floodplain was progressively submerged due to the rising sea level and turned into an estuary (Fig. 8b). During this time span, the loss of their fields, raw materials and freshwater springs may have forced Neolithic people to migrate to a safer location upland, as reported for several places in the Peloponnese at this period (Weiberg et al. 2016). We hypothesise that they have settled further north, for instance in Lambayanna Bay, where the Bronze Age settlement has been identified (Beck and Koutsoumba 2015).

6 Conclusion

In this study, we propose a reconstruction of the landscape evolution in Kiladha Bay from the Late Glacial to Early Holocene shelf exposure to the present, based on multi-beam swath-bathymetry, single-channel chirp seismic profiles and the petrophysical, sedimentological and geochemical analysis of sediment cores, together with AMS ^{14}C-dating. We infer that between ~ 8500 and 6300 cal year BP, the landscape was influenced by fluvial processes that possibly led to the establishment of an estuarine system. The accumulation of fine-grained estuarine sediments filled the accommodation space of the valley, converting it into a partly submerged area, which enabled the formation of paralic swamps, as witnessed by reduced sediments containing root remains. Around ~ 6300 cal year BP, the marine transgression reached the area of investigation, as recognised in the seismic data by a high-amplitude reflection, and in the cores at ~ 10.8 mbsl by a shell-rich layer reflecting a beach environment. The respective elevation is ~ 7.7 m deeper than the global sea level at that time, indicating tectonic subsidence in the Argolic Gulf. Inferred, variable subsidence rates in adjacent locations are compatible with the presence of active faults cutting across the gulf. The rising sea level buried these shell-rich deposits under fine-grained shallow marine sediments and caused a landward migration of the shoreline. We interpret the unexpected enrichment in shells and pebbles in the top decimetres of the sediment sequence as anthropogenic dropstones from various human activities. Moreover, an apparent eutrophication in the last decades is indicated by darker colour and increase in OM in the topmost sediments.

As already suggested by van Andel (1987), the prior to 6300 years exposed terrace at the north of the river valley could present excellent conditions for a Neolithic village, due to the nearby presence of freshwater springs and the availability of clay material for pottery. The retrieval of a Neolithic pottery sherd and other archaeological artefacts reinforce this hypothesis. The rising sea level may have forced Neolithic people to migrate to a safer location, for instance to Lambayanna Bay, where a Bronze Age settlement has been recently discovered (Beck and Koutsoumba 2015). Future investigations on the submerged terrace offshore Franchthi Cave, as well as in other submerged terraces southwards or northwards of Franchthi Cave, such as in Lambayanna Bay, will contribute to a better understanding of the interactions between human developments and sea-level changes as well as tectonic processes around Kiladha Bay.

Acknowledgements We would like to thank all the people who helped us for the coring in Greece, as well as K. D. Vitelli for her identification of Neolithic pottery, Erika Gobet for identifying some of the biological remains, and Eike Neubert for his expertise in molluscs. We are grateful to Julijana Krbanjevic for the CNS analysis, Nicole Schwendener for the CT-scanning and Sönke Szidat for the AMS ^{14}C-dating. We also thank the two anonymous reviewers for the constructive improvements.

References

Ariztegui, D., Asioli, A., Lowe, J. J., Trincardi, F., Vigliotti, L., Tamburini, F., et al. (2000). Palaeoclimate and the formation of sapropel S1: Inferences from Late Quaternary lacustrine and marine sequences in the central Mediterranean region. *Palaeogeography, Palaeoclimatology, Palaeoecology, 158,* 215–240.

Avramidis, P., Iliopoulos, G., Nikolaou, K., Kontopoulos, N., Koutsodendris, A., & van Wijngaarden, G. J. (2017). Holocene sedimentology and coastal geomorphology of Zakynthos Island, Ionian Sea: A history of a divided Mediterranean island.

Palaeogeography, Palaecolimatology, Palaecoecology, 487, 340–354.

Bailey, G. N., & Flemming, N. C. (2008). Archaeology of the continental shelf: Marine resources, submerged landscapes and underwater archaeology. *Quaternary Science Reviews, 27,* 2153–2165.

Bannert, D. (1977). *Geological map of Greece, 1/50000, Lighourion sheet*. Athens: Institute of Geological and Mineral Exploration (IGME).

Beck, J., & Koutsoumba, D. (2015). Baie de Kiladha 2014: Expédition Terra Submersa. *Antike Kunst, 58,* 187–190.

Beck, J., & Koutsoumba, D. (2016). Baie de Kiladha 2015. *Antike Kunst, 59,* 153–156.

Beck, J., & Koutsoumba, D. (2017). Baie de Kiladha 2016. *Antike Kunst, 60,* 164–167.

Beck, J., Sakellariou, D., & Koutsoumba, D. (2017). Submerged Neolithic landscapes off Franchthi Cave: The measurements from the Terra Submersa expedition and their implications. In A. Sarris, E. Kalogiropoulou, T. Kalayci, & L. Karimali (Eds.), *Communities, Landscapes, and Interaction in Neolithic Greece. Proceedings of International Conference, Rethymno 29-30 May 2015* (pp. 261–268). Ann Arbor, MI: International Monographs in Prehistory.

Berger, J.-F., & Guilaine, J. (2009). The 8200 cal BP abrupt environmental change and the Neolithic transition: A Mediterranean perspective. *Quaternary International, 200,* 31–49.

Blaauw, M., & Christen, J. A. (2011). Flexible paleoclimate age-depth models using an autoregressive gamma process. *Bayesian Analysis, 6*(3), 457–474.

Bonsall, C., Macklin, M. G., Payton, R. W., & Boroneant, A. (2002). Climate, floods and river gods: Environmental change and the Meso-Neolithic transition in southeast Europe. *Before Farming: The archaeology of Old World hunter-gatherers, 3–4*(2), 1–15.

Bruins, H. J., van der Plicht, J., & MacGillivray, J. A. (2009). The Minoan Santorini eruption and tsunami deposits in Palaikastro (Crete): Dating by geology, archaeology, ^{14}C, and Egyptian chronology. *Radiocarbon, 51*(2), 397–411.

Carlier, A., Riera, P., Amouroux, J.-M., Bodiou, J.-Y., Desmalades, M., & Grémare, A. (2009). Spatial heterogeneity in the food web of a heavily modified Mediterranean coastal lagoon: Stable isotope evidence. *Aquatic Biology, 5,* 167–179.

Croudace, I. W., Rindby, A., & Rothwell, R. G. (2006). ITRAX: Description and evaluation of a new multi-function X-ray core scanner. In R. G. Rothwell (Ed.), *New techniques in sediment core analysis* (pp. 51–63). London: Geological Society, Special Publications, 267.

Dearing, J. (1999). *Environmental magnetic susceptibility: Using the Bartington MS2 System* (2nd ed., p. 54). Kenilworth: Chi.

Farrand, W. R. (2000). *Excavations at Franchthi Cave, Greece. Fascicle 12, Depositional history of Franchthi Cave: Sediments, stratigraphy, and chronology. With a report on the background of the Franchthi Project by Thomas W. Jacobsen* (p. 135). Bloomington and Indianapolis: Indiana University Press.

Friedrich, W. L., Kromer, B., Friedrich, M., Heinemeier, J., Pfeiffer, T., & Talamo, S. (2006). Santorini eruption radiocarbon dated to 1627–1600 B.C. *Science, 312,* 548.

Gaitanakis, P., & Fotiades, A. (2007). *Geological map of Greece, 1/50000, Spetses-Spetsopoula sheet*. Athens: Institute of Geological and Mineral Exploration (IGME).

Gifford, J. (1983). Core sampling of a Holocene marine sedimentary sequence and underlying Neolithic cultural material off Franchthi Cave, Greece. In P. M. Masters & N. C. Flemming (Eds.), *Quaternary coastlines and marine archaeology: Towards the Prehistory of land bridges and continental shelves* (pp. 269–281). London: Academic.

Gooday, A. J., Jorissen, F., Jorissen, F., Levin, L. A., Middelburg, J. J., Naqvi, S. W. A., et al. (2009). Historical records of coastal eutrophication-induced hypoxia. *Biogeosciences, 6,* 1–39.

Karageorgis, A. P., Anagnostou, C. L., Sioulas, A. I., Kassoli-Fournaraki, A. E., & Eleftheriadis, G. E. (1997). Sedimentology and geochemistry of surface sediments in a semi-enclosed marine area, Central Aegean-Greece. *Oceanologica Acta, 20*(3), 513–520.

Kylander, M. E., Klaminder, J., Wohlfarth, B., & Löwemark, L. (2013). Geochemical responses to paleoclimatic changes in southern Sweden since the Late Glacial: The Hässeldala Port lake sediment record. *Journal of Paleolimnology, 50,* 57–70.

Lambeck, K. (1996). Sea-level change and shore-line evolution in Aegean Greece since Upper Palaeolithic time. *Antiquity, 70*(269), 588–611.

Lambeck, K., Rouby, H., Purcell, A., Sun, Y., & Sambridge, M. (2014). Sea level and global ice volumes from the Last Glacial Maximum to the Holocene. *Proceedings of the National academy of Sciences of the United States of America, 111*(43), 15296–15303.

Löwemark, L., Chen, H.-F., Yang, T.-N., Kylander, M., Yu, E.-F., Hsu, Y.-W., et al. (2011). Normalizing XRF-scanner date: A cautionary note on the interpretation of high-resolution records from organic-rich lakes. *Journal of Asian Earth Sciences, 40,* 1250–1256.

Meyers, P. A. (1997). Organic geochemical proxies of paleoceanographic, paleolimnologic, and paleoclimatic processes. *Organic Geochemistry, 27*(5/6), 213–250.

Meyers, P. A., & Teranes, J. L. (2001). Sediment organic matter. In W. M. Last & J. P. Smol (Eds.), *Tracking environmental change using lake sediments. Physical and geochemical methods* (Vol. 2, pp. 239–270). Dordrecht: Kluwer Academic.

Minoura, K., Imamura, F., Kuran, U., Nakamura, T., Papadopoulos, G. A., Takahashi, T., et al. (2000). Discovery of Minoan tsunami deposits. *Geology, 28*(1), 59–62.

Mourtzas, N. D., & Kolaiti, E. (2013). Historical coastal evolution of the ancient harbor of Aegina in relation to the Upper Holocene relative sea level changes in the Saronic Gulf, Greece. *Palaeogeography, Palaeoclimatology, Palaeoecology, 392,* 411–425.

Ntageretzis, K., Vött, A., Fischer, P., Hadler, H., Emde, K., Röbke, B. R., et al. (2015a). Palaeotsunami history of the Elos plain (Evrotas River delta, Peloponnese, Greece). *Zeitschrift für Geomorphologie, Supplementary Issues, 59*(4), 253–273.

Ntageretzis, K., Vött, A., Fischer, P., Hadler, H., Emde, K., Röbke, B. R., et al. (2015b). Traces of repeated tsunami landfall in the vicinity of Limnothalassa Moustou (Gulf of Argolis—Peloponnese, Greece). *Zeitschrift für Geomorphologie, Supplementary Issues, 59*(4), 301–317.

Papadopoulos, G. A., Gràcia, E., Urgeles, R., Sallares, V., De Martini, P. M., Pantosti, D., et al. (2014). Historical and pre-historical tsunamis in the Mediterranean and its connected seas: Geological signatures, generation mechanisms and coastal impacts. *Marine Geology, 354,* 81–109.

Pavlopoulos, K., Fouache, E., Sidiropoulou, M., Triantaphyllou, M., Vouvalidis, K., Syrides, G., et al. (2013). Palaeoenvironmental evolution and sea-level changes in the coastal area of NE Lemnos Island (Greece) during the Holocene. *Quaternary International, 308–309,* 80–88.

Perlès, C., Quiles, A., & Valladas, H. (2013). Early seventh-millennium AMS dates from domestic seeds in the Initial Neolithic at Franchthi Cave (Argolid, Greece). *Antiquity, 87,* 1001–1015.

Pribyl, D. W. (2010). A critical review of the conventional SOC to SOM conversion factor. *Geoderma, 156,* 75–83.

Reimer, P. J., Bard, E., Bayliss, A., Beck, J. W., Blackwell, P. G., Bronk Ramsey, C., et al. (2013). IntCal13 and Marine13

radiocarbon age calibration curves of 0–50,000 years cal BP. *Radiocarbon, 55*(4), 1869–1887.

Rotzoll, K., & Fletcher, C. H. (2013). Assessment of groundwater inundation as a consequence of sea-level rise. *Nature Climate Change, 3,* 477–481.

Sakellariou, D., Beck, J., Rousakis, G., Georgiou, P., Panagiotopoulos, I., Morfis, I., Tsampouraki-Kraounaki, K., Zavitsanou, A. (2015). Submerged prehistoric landscapes off Franchthi Cave, East Argolic Gulf: Preliminary results. *11th Panhellenic Symposium on Oceanography and Fisheries, Proceedings*, pp. 993–996.

Sakellariou, D., & Galanidou, N. (2015). Pleistocene submerged landscapes and Palaeolithic archaeology in the tectonically active Aegean region. In J. Harff, G. Bailey, & F. Lüth (Eds.), *Geology and archaeology: Submerged landscapes of the continental shelf* (pp. 145–178). London: Geological Society, Special Publications, 411.

Sandgren, P., & Snowball, I. (2001). Application of mineral magnetic techniques to paleolimnology. In W. M. Last & J. P. Smol (Eds.), *Tracking environmental change using lake sediments. Physical and geochemical methods* (Vol. 2, pp. 217–238). Dordrecht: Kluwer Academic.

Simmons, A. H. (2007). *The Neolithic revolution in the Near East: Transforming the human landscape* (p. 360). Tucson: University of Arizona Press.

Stuiver, M., & Polach, H. A. (1977). Discussion: Reporting of ^{14}C data. *Radiocarbon, 19*(3), 355–363.

Tjallingii, R., Röhl, U., Kölling, M., & Bickert, T. (2007). Influence of the water content on X-ray fluorescence core-scanning measurements in soft marine sediments. *Geochemistry, Geophysics, Geosystems, 8*(2), Q02004. https://doi.org/10.1029/2006gc001393.

van Andel, T. H. (1987). The landscape. In T. H. van Andel & S. B. Sutton (Eds.), *Excavations at Franchthi Cave, Greece. Fascicle 2, Landscape and people of the Franchthi region. With contributions by Julie M. Hansen and Charles J. Vitaliano* (pp. 3–62). Bloomington and Indianapolis: Indiana University Press.

van Andel, T. H. (1989). Late Quaternary sea-level changes and archaeology. *Antiquity, 63,* 733–745.

van Andel, T. H., Jacobsen, T. W., Jolly, J. B., & Lianos, N. (1980). Late Quaternary history of the coastal zone near Franchthi Cave, southern Argolid, Greece. *Journal of Field Archaeology, 7*(4), 389–402.

van Andel, T. H., & Lianos, N. (1983). Prehistoric and historic shorelines of the southern Argolid peninsula: A subbottom profiler study. *International Journal of Nautical Archaeology and Underwater Exploration, 12*(4), 303–324.

Vitaliano, C. J. (1987). Plate 1: Geology of Ermioni basin and environs, Peloponnesos, Greece. In T. W. Jacobsen & W. R. Farrand (Eds.), *Excavations at Franchthi Cave, Greece. Fascicle 1, Franchthi Cave and Paralia: Maps, plans, and sections. With contributions by F.A. Cooper and C.J. Vitaliano (Plate 1)*. Bloomington and Indianapolis: Indiana University Press.

Vogel, H., Wagner, B., Zanchetta, G., Sulpizio, R., & Rosén, P. (2010). A paleoclimate record with tephrochronological age control for the last glacial-interglacial cycle from Lake Ohrid, Albania and Macedonia. *Journal of Paleolimnology, 44,* 295–310.

Vött, A. (2007). Relative sea level changes and regional tectonic evolution of seven coastal areas in NW Greece since the mid-Holocene. *Quaternary Science Reviews, 26,* 894–919.

Weiberg, E., Unkel, I., Kouli, K., Holmgren, K., Avramidis, P., Bonnier, A., et al. (2016). The socio-environmental history of the Peloponnese during the Holocene: Towards an integrated understanding of the past. *Quaternary Science Reviews, 136,* 40–65.

Wentworth, C. K. (1922). A scale of grade and class terms for clastic sediments. *The Journal of Geology, 30*(5), 377–392.

Wilkinson, T. J., & Duhon, S. T. (1990). *Excavations at Franchthi Cave, Greece. Fascicle 6, Franchthi Paralia: The sediments, stratigraphy, and offshore investigations. With contributions by John A. Gifford and Sytze Bottema* (p. 207). Bloomington and Indianapolis: Indiana University Press.